PROCEEDINGS OF SPIE

Infrared Technology and Applications XLII

Bjørn F. Andresen
Gabor F. Fulop
Charles M. Hanson
Paul R. Norton
Editors

18–21 April 2016
Baltimore, Maryland, United States

Sponsored and Published by
SPIE

Volume 9819

Proceedings of SPIE 0277-786X, V. 9819

SPIE is an international society advancing an interdisciplinary approach to the science and application of light.

Infrared Technology and Applications XLII, edited by Bjørn F. Andresen,
Gabor F. Fulop, Charles M. Hanson, Paul R. Norton, Proc. of SPIE Vol. 9819,
981901 · © 2016 SPIE · CCC code: 0277-786X/16/$18 · doi: 10.1117/12.2244347

The papers in this volume were part of the technical conference cited on the cover and title page. Papers were selected and subject to review by the editors and conference program committee. Some conference presentations may not be available for publication. Additional papers and presentation recordings may be available online in the SPIE Digital Library at SPIEDigitalLibrary.org.

The papers reflect the work and thoughts of the authors and are published herein as submitted. The publisher is not responsible for the validity of the information or for any outcomes resulting from reliance thereon.

Please use the following format to cite material from this book:
Author(s), "Title of Paper," in *Infrared Technology and Applications XLII*, edited by Bjørn F. Andresen, Gabor F. Fulop, Charles M. Hanson, Paul R. Norton, Proceedings of SPIE Vol. 9819 (SPIE, Bellingham, WA, 2016) Six-digit Article CID Number.

ISSN: 0277-786X
ISSN: 1996-756X (electronic)
ISBN: 9781510600607

Published by
SPIE
P.O. Box 10, Bellingham, Washington 98227-0010 USA
Telephone +1 360 676 3290 (Pacific Time) · Fax +1 360 647 1445
SPIE.org

Copyright © 2016, Society of Photo-Optical Instrumentation Engineers.

Copying of material in this book for internal or personal use, or for the internal or personal use of specific clients, beyond the fair use provisions granted by the U.S. Copyright Law is authorized by SPIE subject to payment of copying fees. The Transactional Reporting Service base fee for this volume is $18.00 per article (or portion thereof), which should be paid directly to the Copyright Clearance Center (CCC), 222 Rosewood Drive, Danvers, MA 01923. Payment may also be made electronically through CCC Online at copyright.com. Other copying for republication, resale, advertising or promotion, or any form of systematic or multiple reproduction of any material in this book is prohibited except with permission in writing from the publisher. The CCC fee code is 0277-786X/16/$18.00.

Printed in the United States of America.

Publication of record for individual papers is online in the SPIE Digital Library.

SPIE. DIGITAL LIBRARY
SPIEDigitalLibrary.org

Paper Numbering: Proceedings of SPIE follow an e-First publication model, with papers published first online and then in print. Papers are published as they are submitted and meet publication criteria. A unique citation identifier (CID) number is assigned to each article at the time of the first publication. Utilization of CIDs allows articles to be fully citable as soon as they are published online, and connects the same identifier to all online, print, and electronic versions of the publication. SPIE uses a six-digit CID article numbering system in which:

- The first four digits correspond to the SPIE volume number.
- The last two digits indicate publication order within the volume using a Base 36 numbering system employing both numerals and letters. These two-number sets start with 00, 01, 02, 03, 04, 05, 06, 07, 08, 09, 0A, 0B … 0Z, followed by 10-1Z, 20-2Z, etc.

The CID Number appears on each page of the manuscript. The complete citation is used on the first page, and an abbreviated version on subsequent pages.

Contents

IR IN AIR AND SPACE

SELECTED APPLICATIONS

TYPE II SUPERLATTICE FPAS I

TYPE II SUPERLATTICE FPAS II

FPA SUBSTRATES

QWIP AND CQD

HOT: HIGH-OPERATING TEMPERATURE FPAS I

HOT: HIGH-OPERATING TEMPERATURE FPAS II

UNCOOLED FPAS AND APPLICATIONS

HGCDTE

WORDS FROM THE MASTER

SMART PROCESSING I

SMART PROCESSING II

Authors

Numbers in the index correspond to the last two digits of the six-digit citation identifier (CID) article numbering system used in Proceedings of SPIE. The first four digits reflect the volume number. Base 36 numbering is employed for the last two digits and indicates the order of articles within the volume. Numbers start with 00, 01, 02, 03, 04, 05, 06, 07, 08, 09, 0A, 0B...0Z, followed by 10-1Z, 20-2Z, etc.

Conference Committee

Symposium Chair

David A. Logan, BAE Systems (United States)

Symposium Co-chair

Donald A. Reago Jr., U.S. Army Night Vision & Electronic Sensors Directorate (United States)

Conference Chairs

Bjørn F. Andresen, RICOR-Cryogenic & Vacuum Systems (Israel)
Gabor F. Fulop, Maxtech International, Inc. (United States)
Charles M. Hanson, SenseIR Solutions, LLC (United States)
Paul R. Norton, U.S. Army Night Vision & Electronic Sensors Directorate (United States)

Conference Program Committee

Tayfun Akin, Mikro-Tasarim Ltd. (Turkey) and Middle East Technical University (Turkey)
Stefan T. Baur, Raytheon Vision Systems (United States)
Philippe F. Bois, Thales Research & Technology (France)
Wolfgang A. Cabanski, AIM INFRAROT-MODULE GmbH (Germany)
John T. Caulfield, Cyan Systems (United States)
Eric Costard, IRnova AB (Sweden)
Ronald G. Driggers, St. Johns Optical Systems (United States)
Michael T. Eismann, Air Force Research Laboratory (United States)
Mark E. Greiner, L-3 Communications Cincinnati Electronics (United States)
Sarath D. Gunapala, Jet Propulsion Laboratory (United States)
Weida Hu, Shanghai Institute of Technical Physics (China)
Masafumi Kimata, Ritsumeikan University (Japan)
Hee Chul Lee, KAIST (Korea, Republic of)
Paul D. LeVan, Air Force Research Lab. (United States)
Kevin C. Liddiard, Electro-optic Sensor Design (Australia)
Wei Lu, Shanghai Institute of Technical Physics (China)
Tara J. Martin, UTC Aerospace Systems (United States)
Paul L. McCarley, Air Force Research Laboratory (United States)
R. Kennedy McEwen, SELEX ES (United Kingdom)
John Lester Miller, Cascade Electro Optics LLC (United States)
A. Fenner Milton, U.S. Army RDECOM CERDEC NVESD (United States)

Mario O. Münzberg, Airbus Defence and Space (Germany)
Peter W. Norton, BAE Systems (United States)
Robert A. Owen, L-3 Communications EOTech (United States)
Joseph G. Pellegrino, U.S. Army Night Vision & Electronic Sensors Directorate (United States)
Vladimir P. Ponomarenko, Orion Research-and-Production Association (Russian Federation)
Manijeh Razeghi, Northwestern University (United States)
Donald A. Reago Jr., U.S. Army RDECOM CERDEC NVESD (United States)
Colin E. Reese, U.S. Army Night Vision & Electronic Sensors Directorate (United States)
Patrick Robert, ULIS (France)
Antoni Rogalski, Military University of Technology (Poland)
Thomas R. Schimert, DRS Technologies, Inc. (United States)
Itay Shtrichman, SCD Semiconductor Devices (Israel)
Torbjørn Skauli, Norwegian Defence Research Establishment (Norway)
Rengarajan Sudharsanan, Spectrolab, Inc., A Boeing Company (United States)
Stefan P. Svensson, U.S. Army Research Laboratory (United States)
J. Ralph Teague, Georgia Tech Research Institute (United States)
William A. Terre, FLIR Systems, Inc. (United States)
Simon Thibault, University Laval (Canada)
Meimei Tidrow, U.S. Army Night Vision & Electronic Sensors Directorate (United States)
Michel Vuillermet, SOFRADIR (France)
James R. Waterman, U.S. Naval Research Laboratory (United States)
Lucy Zheng, Institute for Defense Analyses (United States)

Session Chairs

1 NIR/SWIR FPAs and Applications
Mario O. Münzberg, Airbus Defence and Space (Germany)
Tara J. Martin, Sensors Unlimited, a United Technologies Company (United States)

2 IR in Air and Space
John Lester Miller, Cascade Electro Optics LLC (United States)
R. Kennedy McEwen, SELEX ES Infrared Ltd. (United Kingdom)

3 Selected Applications
Torbjørn Skauli, Norwegian Defence Research Establishment (Norway)

4 Type II Superlattice FPAs I
Meimei Tidrow, U.S. Army Night Vision & Electronic Sensors Directorate (United States)
Lucy Zheng, Institute for Defense Analyses (United States)
Manijeh Razeghi, Northwestern University (United States)

5 Type II Superlattice FPAs II
Meimei Tidrow, U.S. Army Night Vision & Electronic Sensors Directorate (United States)
Lucy Zheng, Institute for Defense Analyses (United States)
Manijeh Razeghi, Northwestern University (United States)

6 Keynote Session: Joint session with conferences 9819, 9821, 9822
Paul R. Norton, U.S. Army Night Vision & Electronic Sensors Directorate (United States)

7 FPA Substrates
Eric Costard, IRnova AB (Sweden)

8 QWIP and CQD
Eric Costard, IRnova AB (Sweden)

9 HOT: High-Operating Temperature FPAs I
David Z. Ting, Jet Propulsion Laboratory (United States)
Philip C. Klipstein, SCD SemiConductor Devices (Israel)

10 HOT: High-Operating Temperature FPAs II
Avraham R. Fraenkel, SCD SemiConductor Devices (Israel)
Adam Piotrowski, VIGO System S.A. (Poland)

11 Uncooled FPAs and Applications
Kevin C. Liddiard, Electro-optic Sensor Design (Australia)
Michael Groenert, U.S. Army Night Vision & Electronic Sensors Directorate (United States)

12 HgCdTe
Michael Groenert, U.S. Army Night Vision & Electronic Sensors Directorate (United States)
David Billon-Lanfrey, SOFRADIR (France)

13 Words from the Master
Paul R. Norton, U.S. Army Night Vision & Electronic Sensors Directorate (United States)

14 Smart Processing I
John T. Caulfield, Cyan Systems (United States)
Paul L. McCarley, Air Force Research Laboratory (United States)

15 Smart Processing II
John T. Caulfield, Cyan Systems (United States)
Paul L. McCarley, Air Force Research Laboratory (United States)

Introduction

The Forty-Second conference on Infrared Technology and Applications was held the week of April 18-21, 2016 at the Baltimore Convention Center in Baltimore, Maryland. The agenda was divided into 15 sessions:

1. NIR/SWIR FPAs and Applications
2. Infrared in Air and Space
3. Selected Applications
4. Type II Superlattice FPAs I
5. Type II Superlattice FPAs II
6. Keynote
7. FPA Substrates
8. QWIP and CQD
9. HOT: High Operating Temperature FPAs I
10. HOT: High Operating Temperature FPAs II
11. Uncooled FPAs and Applications I
12. HgCdTe
13. A Word from the Master
14. Smart Processing I
15. Smart Processing II

Note that two new conferences have been initiated to cover the topics of optics (Advanced Optics for Defense Applications: UV through LWIR) and coolers (Tri-Technology Device Refrigeration) that were previously part of this conference.

In addition, there were a number of poster papers presented for discussion on Tuesday evening—these have been added to the 15 sessions in the Proceedings. Highlights of five topical areas are summarized below:

- Photon Detectors
- Uncooled Detectors
- Smart Processing
- Applications
- Keynote Address

Photon Detectors

NIR/SWIR FPAs and Applications

A number of trends were emphasized in near infrared and shortwave infrared in presentations at this conference:

- The continuing emphasis on InGaAs FPAs in which pixel sizes have been reduced to 10 μm and operation has been achieved without a thermoelectric cooler over a wide temperature range.
- Extended wavelength operation which has been demonstrated in InGaAs, HgCdTe and T2SL (Type 2 Superlattice) SWIR FPAs.
- In the NIR spectrum, imagers made with ultra-fast-laser-processed “black silicon” combined with low-noise backside illuminated CMOS, have achieved enhanced quantum efficiencies and low-light-level sensitivities below 1 mLux at 60 Hz.

In order to address the power consumption problem, one manufacturer developed a camera without a Thermo-Electric Cooler (TEC-less) 640 × 512 InGaAs camera with temperature-based non uniformity corrections that allow the power consumption to be 1.2 to 1.3 W over a -30 to 60 °C temperature range—see Fig. 1.

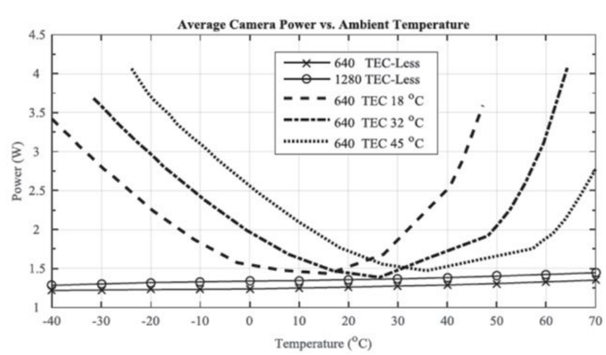

Fig. 1 Power vs. temperature comparing the TEC-less camera and the TEC variant.

Fig. 2 SWIR image with an existing 10 µm ROIC.

A 1280 × 1024 InGaAs FPA with 10 μm pixels and an asynchronous laser pulse detection mode has been fabricated, thus providing both passive and active imaging in low-light-level conditions. An image from this FPA is shown in Figure 2.

The latest results on an innovative InGaAs/GaAsSb T2SL SWIR FPA with 2.35 μm cutoff were reported. Dark currents were less than for SWIR HgCdTe FPAs. With thicker InGaAs the cutoff can be extended to 2.55 μm.

In other SWIR superlattice work, $InAs/InAs_{1-x}Sb_x/AlAs_{1-x}Sb_x$ T2SL SWIR detectors on GaSb substrates, had a dark current density of 1.3×10^{-8} A/cm^2 at 200 K, with 36% quantum efficiency.

In HgCdTe, SWIR FPAs with 2.5 μm cutoff, 640 × 512 formats with 15 μm pixels operating in both passive and active modes were demonstrated. These are currently made by means of LPE but for production transfer to MBE on GaAs substrates is expected.

For passive imaging, the dark current in Fig.3 is seen to be less than one order of magnitude higher than that for the empirical Rule 07. Work is ongoing to reduce the dark current further.

For active imaging with APDs (Avalanche PhotoDiodes) special ROICs were designed for Gated Viewing (GV) with a 1.57 μm Nd:YAG laser illuminator

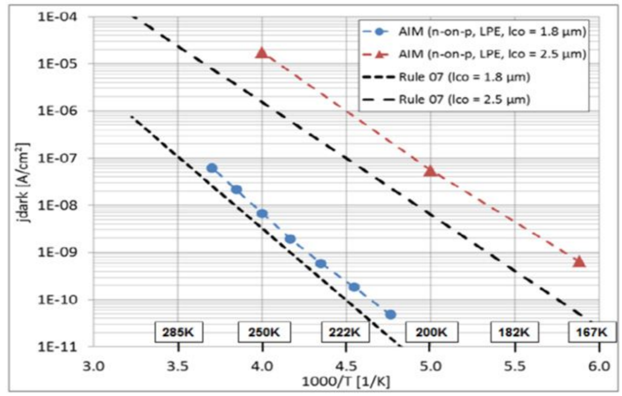

Fig. 3 Dark current density vs. 1/T for 1.8 µm and 2.5 µm cut-off FPAs compared with Rule 07.

Type II superlattice FPAs

There were a total of ten papers in the two sessions devoted to Type II Superlattice and Barrier detectors, and several more on this subject in the Poster session. This reflects the continued strong interest in the potential performance advantages that this technology has been predicted to have theoretically—long carrier lifetimes and a high optical absorption coefficient. Experimentally, lifetimes as long as those predicted have not yet been achieved. Lifetimes are still shorter than for HgCdTe with comparable bandgaps. This year continued a larger focus on LWIR devices.

Passivation of Type II structures using the Gibbs free energy was the focus of the first paper in the topical area. The authors compared ALD-deposited Al_2O_3, HfO_2, TiO_2, ZnO, PECVD deposited SiO_2, Si_3N_4 and sulphur containing octadecanethiol (ODT) self-assembled monolayers (SAM) passivation layers on InAs/GaSb *pin* superlattice photodetectors with cut-off wavelength at 5.1 µm. Fig. 4 shows how the dark current varies with temperature for a variety of passivation choices. Best results were reported for Al_2O_3.

GaSb oxide was investigated with respect to its affect on sidewall leakage for Type II mesa structures. After annealing at temperatures above 300 °C, free Sb was detected on the surfaces that can cause sidewall leakage.

LWIR Type II superlattice development was updated in an important paper that showed R_0A values for test

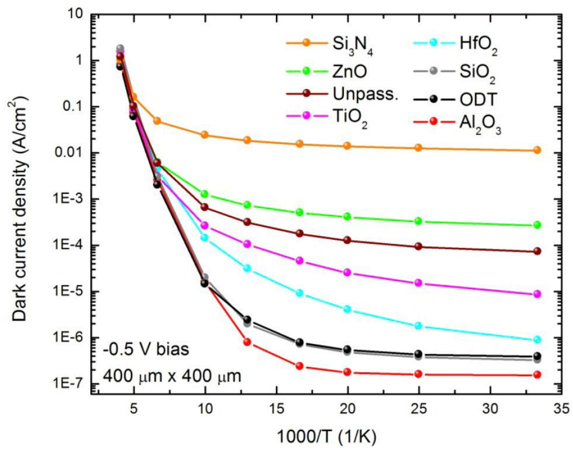

Fig. 4 Temperature dependent dark current density for unpassivated and passivated type-II InAs/GaSb superlattice 400 × 400 μm photodiodes at -0.5 V bias voltage.

structures and test devices clustered around 10 × and 20 × the HgCdTe benchmark Rule 07 as shown in Fig. 5. This development has been achieved with standard InAs/GaSb material that includes a majority-carrier barrier and that has a short lifetime ~30 nsec. Nevertheless, good imagery was shown for a 15 μm pitch 512 × 640 FPA at 77 K having > 50 % quantum efficiency with a 9.3 μm cutoff at f/2.7 as illustrated in Fig. 6.

Asymmetrical MWIR InAs/GaSb superlattice *pin* photodiodes were found to have very short minority-carrier diffusion lengths due to short lifetime of 30-35 nsec, leading to low quantum efficiency. Results were improved to about 42 % quantum efficiency by reversing the side of the structure that was illuminated. Higher QE results were found with test structures having a p-type absorber rather than an n-type absorber, taking advantage of the improved mobility of electrons compared to holes.

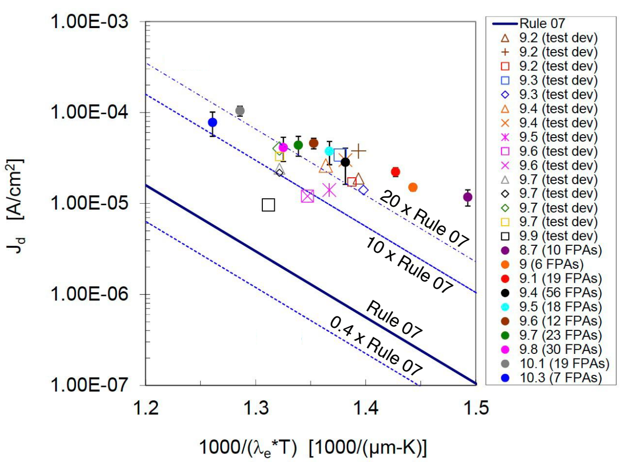

Fig. 5 77 K dark current: comparison of Type II superlattice test devices and FPAs with MCT Rule 07 (solid blue line) over a similar range of cut-off wavelengths

Fig. 6 Image registered with a demonstration camera containing the 15μm pitch, 640 × 512 LW FPA, operating with F/2.7 optics at 77 K and a scene distance of about 5 km.

Development of a 6 μm cutoff MWIR Type II superlattice FPA was described using InAs/GaSb combined with barrier layers. The *pin* structure is illustrated in Fig. 7. The dark current of the *pBiBn* structure was 4 × 10^{-7} A/cm^2 at reverse bias of -20 mV, which is lower than that of the *pin* structure, 7 × 10^{-7} A/cm^2. An FPA with 256 × 320 pixels and a pixel pitch of 30 μm was fabricated and imaged.

An approach for fabricating an antimonide FPA without using indium bumps by employing a membrane-transfer process was described.

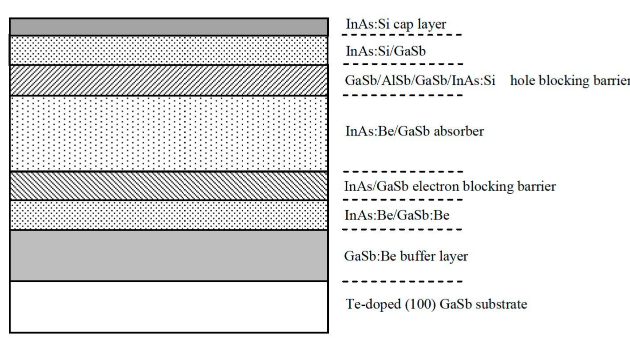

Fig. 7 Epitaxial wafer structure

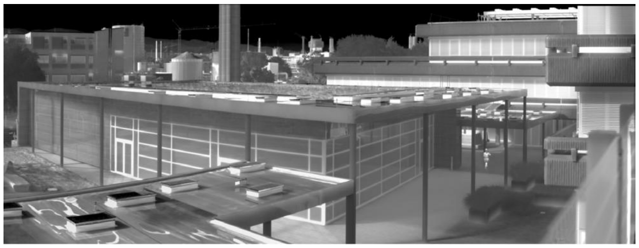

Fig. 8 Image from a 640 × 512 LWIR heterojunction InAs/GaSb T2SL camera with 15 μm pixel pitch.

Recent results with LWIR Type II superlattice FPAs was presented, including a 640 × 512 LWIR heterojunction InAs/GaSb T2SL camera with 15 μm pixel pitch. Fig. 8 illustrates an image from this FPA operated at 55 K and having a cutoff of 10.3 μm.

Ga-free InAs/$InAs_{1-x}Sb_x$ type-II superlattices were reported with LWIR cutoffs and an nBn structure that is illustrated in Fig. 9. With a 6 μm thick absorber, the quantum efficiency was said to be 54 % for a sample with a 50 % cutoff of 10 μm at 77 K. Fig. 10 shows the spectral D* of this LWIR device.

Results from production and development of SWIR, MWIR, and LWIR Type-II superlattice InAs/GaSb detectors was presented. A new large array – see Fig. 11— is being developed in a 1280 × 1024 format with 12 μm pitch and is planned to be available in both MWIR and LWIR bands. Fig. 12 shows the LWIR spectral response.

Dual-band barrier detectors featuring two LWIR bands—9.2 and ~12 μm—was the subject of another presentation. Quantum efficiency for the two bands as a function of bias is shown in Fig. 13.
Large, encapsulant-free GaSb single crystals were

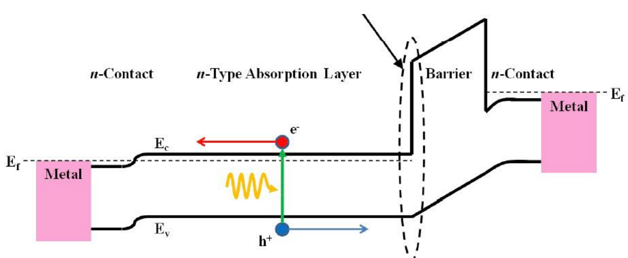

Fig. 9 Schematic diagram and working principle of the nBn photodetector. The barrier blocks the transport of majority electrons, while allowing the diffusion of minority holes and photogenerated carriers from the active region on the left.

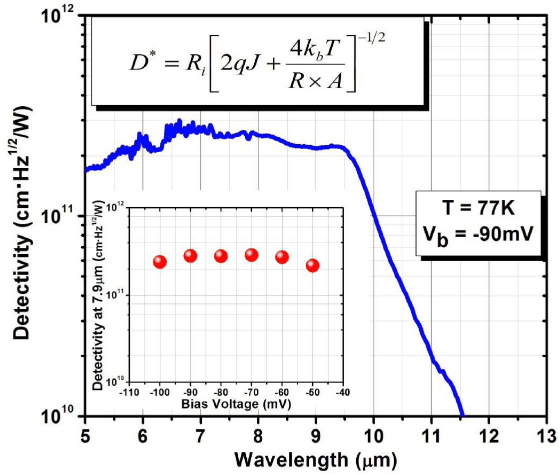

Fig. 10 Detectivity spectrum of the device with a 6 μm-thick absorption region at -90 mV applied bias voltage in front-side illumination configuration without any anti-reflection coating. Inset: Detectivity of the device at 7.9 μm under front-side illumination as a function of applied bias voltage. Detectivity is calculated based on the equation in the inset, where R_i is the device responsivity, J is the dark current density, RA is the resistance-area product, k_b is the Boltzmann constant, and T is the operating temperature.

Fig. 11 Photo of a new Type II superlattice FPA with a resolution of 1280 × 1024 and having 12 μm pitch pixels.

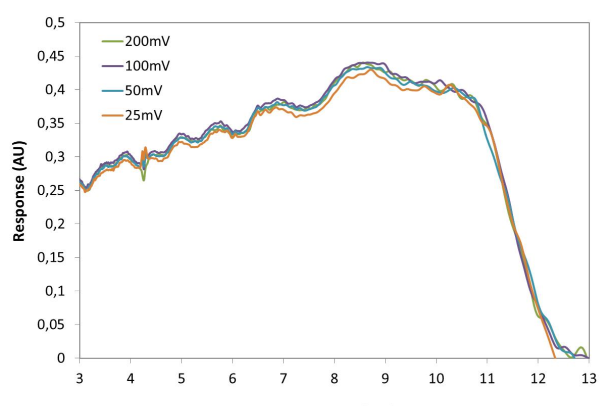

Fig. 12 LWIR Type II spectral response at 77 K as a function of bias, showing that the response is fully turned on already at 25 mV.

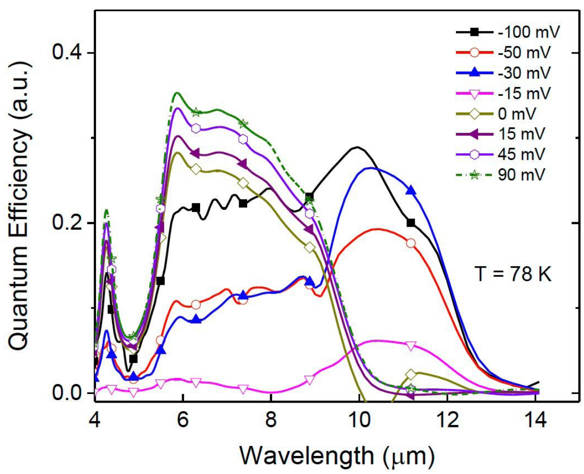

Fig. 13 Bias-dependent QE measurements performed with 6.5 μm and 9.75 μm filters at 78 K.

grown using the modified Czochralski method, yielding more than seventy 150 mm wafers per crystal or several hundred 75 mm or 100 mm wafers per crystal. Fig. 14 shows one of the large boules.

Progress in the development of current substrate polishing techniques has been demonstrated to deliver a consistent, improved surface on GaSb wafers with a readily desorbed oxide for epitaxial growth according to a companion paper. Six wafer polishing variants were compared.

Fig. 14 GaSb boule capable of yielding over 70 6-inch wafers.

InSb crystal growth improvements were described in a paper with a goal of growing 6-inch diameter <111> ingots weighing as much as 30 kg. Reduction of micro-resistivity striations was reported by control of the growth interface.

QWIP and colloidal quantum dot (CQD) detectors

An update was given on the development of resonator QWIP detectors. A quantum efficiency of 37% and conversion efficiency of 15% in a 1.3 μm-thick active material and 35% QE and 21% CE in a 0.6 μm-thick active material. Both detectors have a cutoff at 10.5 μm with a 2 μm bandwidth. The temperature at which photocurrent equals dark current is about 65 K under F/2 optics. The thicker detector shows a large QE polarity asymmetry due to nonlinear potential drop in the QWIP material layers. For one design, an FPA was measured with NEΔT of 27.2 mK, with 99.5% operability at 55 K under F/2.5 optics and 4.46 ms integration time. Fig. 15 shows an image taken with one of these resonator QWIP FPAs.

Fig. 15 Image from a QWIP FPA at V ~ -1.1 V bias and T = 61 K.

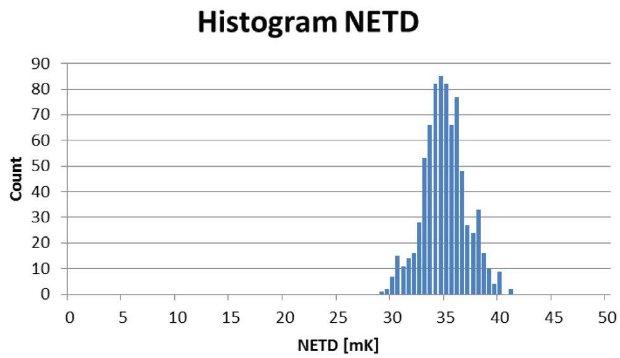

Fig. 16 Distribution of NEΔT for more than 500 production QWIP FPAs in a 640 × 480 format.

QWIP production of FPAs with 640 × 480 and 384 × 288 pixels with 25 μm pitch totaled nearly 200 units in 2015 and are projected to double in 2016. MOVPE was used for the growth of quantum wells on GaAs substrates. Fig. 16 shows a histogram of the NEΔT for production the larger format.

MWIR detection with HgTe colloidal quantum dots was reported. Fig. 17 illustrates the detector concept. Imagery was shown with FPAs made from this material.

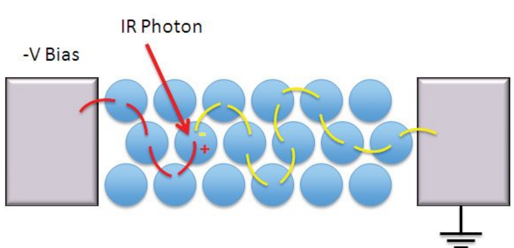

Fig. 17 Diagram of photoconduction in a CQD detector. A photon excites a CQD. The excited electron "hops" from dot-to-dot, generally drifting up the electric field to the anode. The "hole" is filled by electrons that hop up the electric field from the cathode.

High Operating Temperature (HOT) FPAs

The goal of increasing the operating temperature of FPAs without sacrificing performance is motivated by the reduction in cooler power, improved cooler efficiency, longer cooler lifetime, smaller imager size, and lighter weight sensor systems that this makes possible. This goal is being pursued using HgCdTe, Type II superlattices, and *nBn* materials and has relevance especially in the MWIR and LWIR spectral bands.

Planar LWIR and VLWIR HgCdTe detectors in both p-on-n and n-on-p polarities were discussed. Thermal dark currents have been significantly reduced as compared to 'Tennant's Rule 07' in both diode polarities, with quantum efficiency ≥ 60% and for operating temperatures between 30 K and 100 K. Fig. 18 shows the dark current vs. 1/λT. The demonstrated detector performance paves the way for a new generation of higher operating temperature LWIR MCT FPAs with < 30 mK NETD up to a 110 K detector operating temperature and with good operability. This allows for the same dark current performance at a 20 K higher operating temperature than with previous technology.

MWIR XBn detector arrays with 10 μm pitch and a large 1920 × 1536 format were reported. Data for operation up to 150 K with a cutoff of 4.2 μm was shown. The dark current histogram was well behaved at 150 K as shown in Fig. 19.

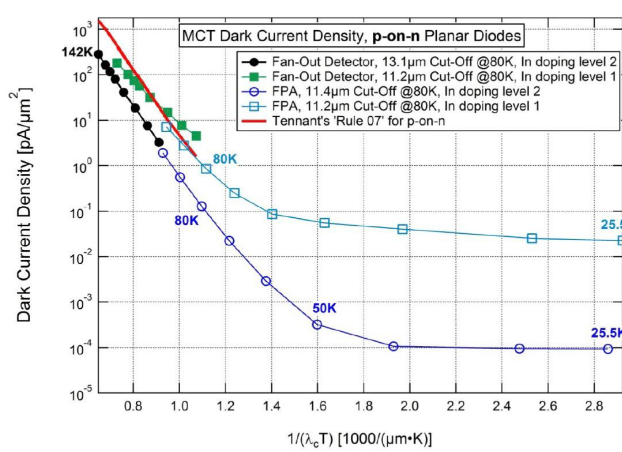

Fig. 18 Thermal dark current density behavior versus 1/λT for p-on-n LWIR and VLWIR MCT detector devices with responsivity cut-off wavelengths at 80 K as stated in the inset. BLIP D* for 5-stage devices with absorption QE of 70%, both under 300 K background with 2π field of view (FOV).

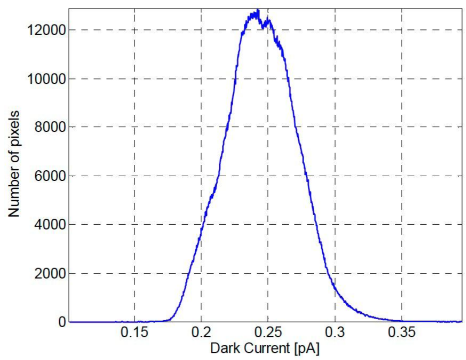

Fig. 19 Histogram of the dark current at 150 K from all pixels of the 1920 × 1536 FPA.

Progress in MOCVD growth of HgCdTe was described, enabling advances in HOT detector operation. Changing the growth orientation from <111> to <100> enabled higher performance operation for 13 μm cutoff photoconductors. In addition, barrier detectors were reported for both MWIR and LWIR bands. An $n^+p^+Bp\pi N^+$ 10 μm cutoff LWIR structure enabled operation with carrier extraction at 230 K. Fig. 20 illustrates this structure.

SWIR Type II superlattice detectors using Ga-free material were reported with operation in the 200 - 300 K range and spectral cutoffs—as shown in Fig. 21—of 1.7 - 1.8 μm. At 300 K, the device exhibited a specific detectivity of 6.45 × 10^{10} Jones with a 300 K 2π field of view.

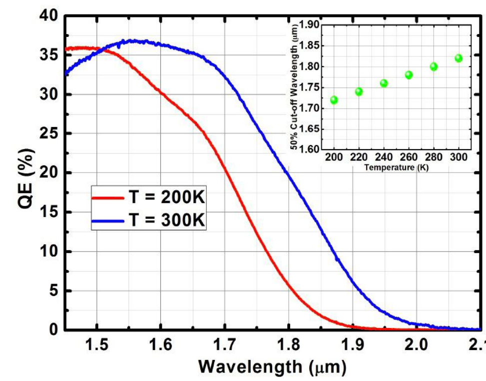

Fig. 21 Saturated 200 and 300 K quantum efficiency spectrum of the device under zero-bias condition in frontside illumination configuration without any anti-reflection coating. Inset: The %50 cut-off wavelength variation of the device vs. temperature between 200 to 300 K.

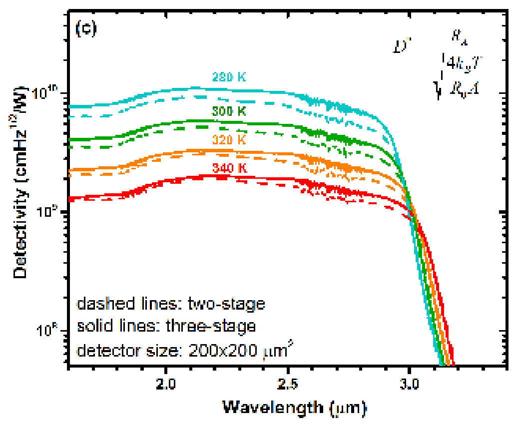

Fig. 22 Johnson-noise limited detectivity for two- and three-stage interband cascade devices.

SWIR interband cascade detectors having a 3 μm cutoff and operating between 280 and 340 K were presented. D* was limited by Johnson noise, as shown in Fig. 22. A mid-wave device was reported to have response approaching 1 GHz.

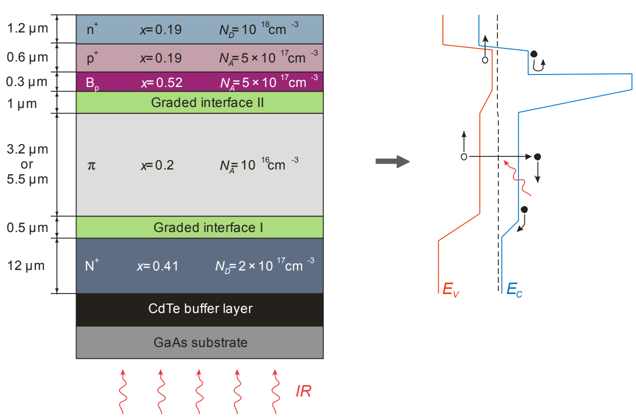

Fig. 20 LWIR $n^+p^+Bp\pi N^+$ HgCdTe structure and schematic photodiode band diagram. x is the alloy composition, N_A is the acceptor concentration, N_D is the donor concentration and π denotes the absorber region with low p-type extrinsic concentration.

Recent developments achieved in terms of HOT MCT extrinsic p on n technology, blue MW band (4.2 μm at 150 K) and extended MW band (5.3 μm at 130 K) were reviewed. Fig. 23 shows the dark current for both red and blue bands vs. temperature compared to Rule 07. This paper also discusses reduction of 1/f noise and the properties of random telegraph noise or signal (RTN or RTS). Fig. 24 shows how the activation energy of RTN noise varies with bandgap.

$In_{0.982}Al_{0.018}Sb$ diodes were fabricated on InSb substrates, followed by mesa diode fabrication. The 4.8 μm cutoff devices were imaged at 80 and 110 K.

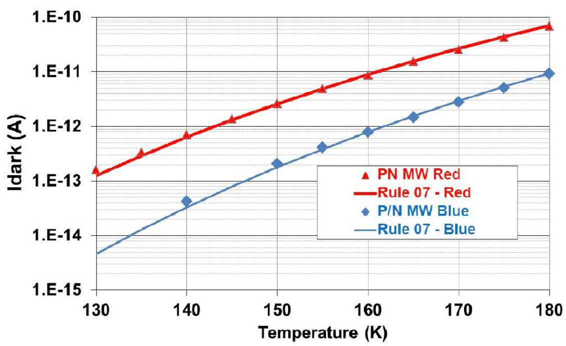

Fig. 23 Mean dark current vs. temperature for MWIR red and blue bands compared with Rule 07.

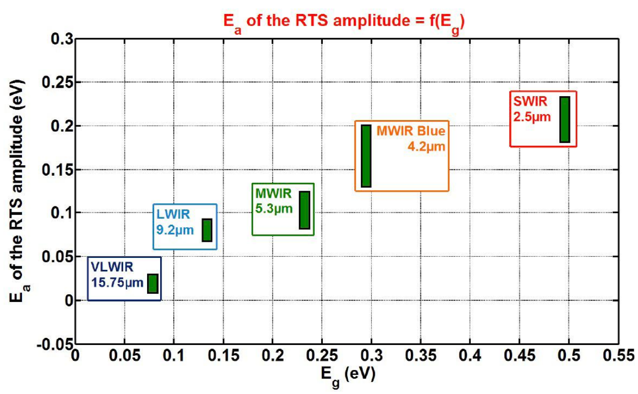

Fig. 24 Random telegraph noise activation energies as a function of the bandgap energy.

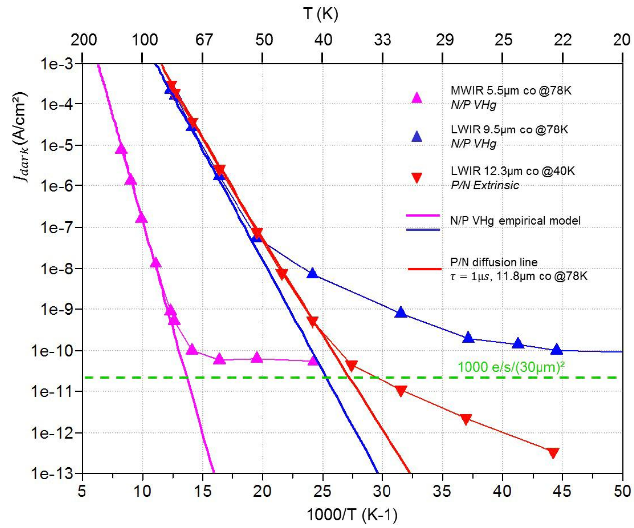

Fig. 25 Arrhenius plot with dark current data for MWIR-LWIR n/p and p/n data

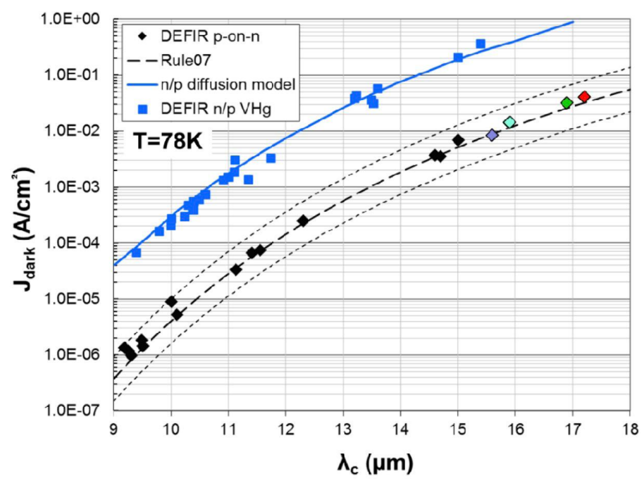

Fig. 26 Summary of dark currents measured at 78K for both n/p and p/n diodes from LWIR up to VLWIR spectral ranges.

HgCdTe

The HgCdTe alloy detector—characterized by a high absorption coefficient and a long lifetime—continues to dominate the choice for a broad range of infrared applications. Aside from applications that are ideal for either InSb in the MWIR spectral band, or InGaAs in the 1.7 µm SWIR band, or those that can utilize uncooled FPAs, HgCdTe continues to be the most popular choice. Papers in this section update how HgCdTe is continuing to develop and evolve. Papers on this topic were presented in the session on HgCdTe detectors as well as in the SWIR and HOT sessions, the Applications sessions, and in the Poster session.

HgCdTe for a variety of space missions was reviewed. This included SWIR bands around 2 - 3 μm for astrophysics, MWIR and LWIR bands for exoplanet discovery, and VLWIR for atmospheric sounding. Fig. 25 shows an arrhenius plot for some MWIR and LWIR devices and for both diode polarities. Fig. 26 shows dark current at 78 K for both diode polarities as a function of the cutoff wavelength.

Progress has been made in the development of 8 μm pitch MOVPE-grown HgCdTe photodiodes in a 1280 × 1024 format. A major effort has gone into raising the operating temperature of these 5+ μm cutoff MWIR devices. Fig. 27 shows the median NEΔT as a function of operating temperature for these FPAs. An image of a container ship taken with this array at ~1.6 km distance using 75 mm f/2.8 optics is shown in Fig. 28. An LWIR FPA based upon this format is under consideration, as well as additional formats, including a full 1080p format array, 4 K × 4 K arrays for surveillance, and smaller formats for handheld applications.

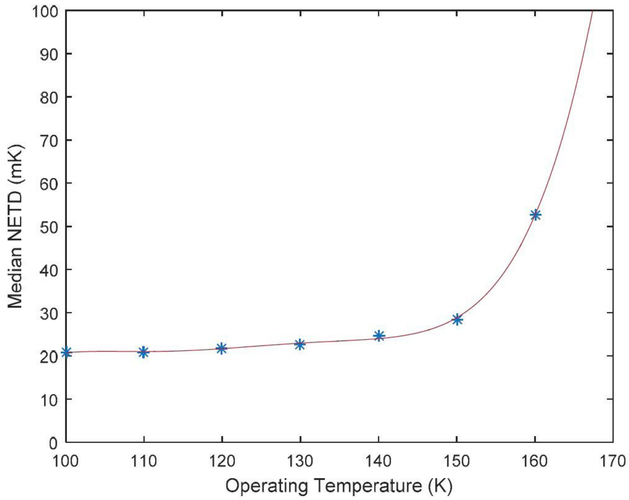

Fig. 27 NEΔT for 1280 × 1024 FPAs having 8 µm pitch pixels at f/2.8 as a function of the operating temperature.

Fig. 28 Image of a container ship at ~ 1.6 km being unloaded taken by an MWIR HgCdTe array with 75 mm f/2.8 optics.

The development of prototype MWIR—5.4 μm cutoff—XGA format (1024 × 768) HgCdTe detector arrays with 10 µm pitch were reported. The associated readout provided 2.8 × 10^6 charge storage in an integrate-while-read mode, and 4.9 × 10^6 for integrate-then-read (ITR) operation. Smaller pixel development for LWIR and 3rd gen is using 12 μm pixels in a 1280 × 720 format. Fig. 29 shows the histogram of an LWIR array in this format. The ITR mode with this larger pixel has a charge storage capacity of 8.3 × 10^6 electrons.

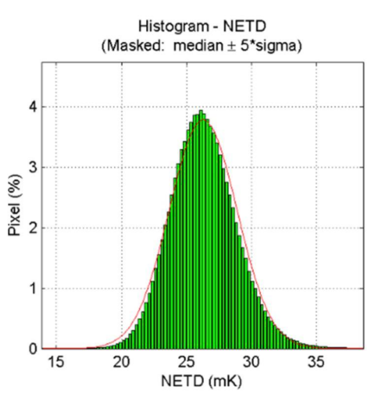

Fig. 29 NEΔT for a 9 μm cutoff array with 12 μm pixels in a 1280 × 720 format.

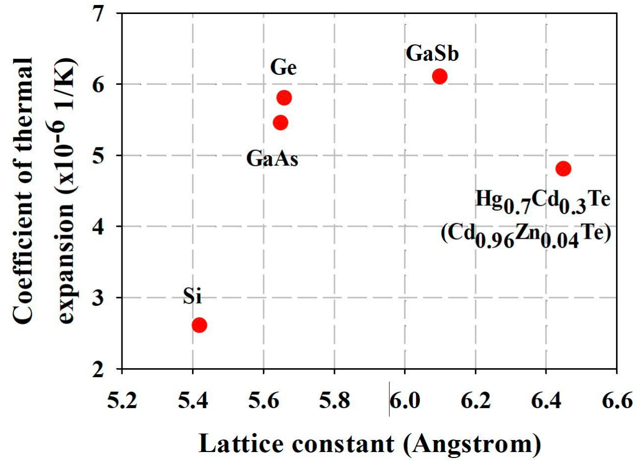

Fig. 30 Lattice and CTE mismatch between HgCdTe and several potential alternative substrates.

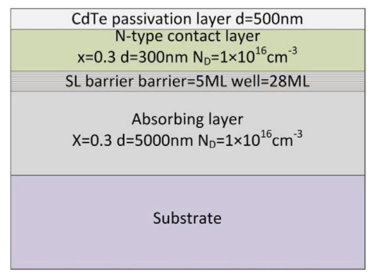

Fig. 31 HgCdTe nBn structure having a superlattice barrier layer.

MBE growth of HgCdTe on GaSb substrates has been explored and compared with growth on GaAs and CdZnTe. Fig. 30 shows the lattice and coefficient of thermal expansion of these materials. GaSb was found to have a lower etch pit density compared to GaAs and comparable X-ray rocking curve value. Device development has concentrated on nBn detector structures. These were grown to compare a solid barrier layer with a superlattice barrier in order minimize the voltage needed to overcome the minority carrier barrier. Fig. 31 shows the structure for the case of a superlattice barrier.

A presentation describing the transition to smaller pitch—15 to 10 μm—was given covering both n-on-p and p-on-n diode polarities. Dark currents were significantly lower for the p-on-n polarity, but the smaller diodes in this case showed excess dark current ~30 %. This may have been due to the test structure design interacting with the long diffusion lengths (25 -30 μm) in this case—see Fig. 32.

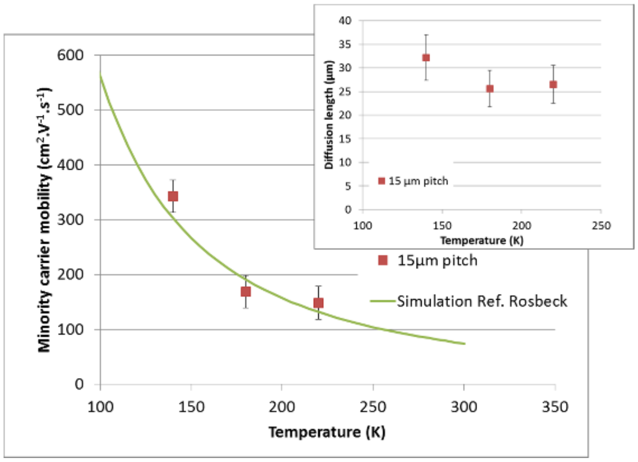

Fig. 32 Extracted minority carrier mobility and minority carrier diffusion lenght (inset) from a LWIR 15 µm pitch array.

VLWIR (12 - 15 μm) photodiodes for atmospheric sounding were studied, as well as electron avalanche photodiodes for high speed and low-flux applications. Excess currents were modeled and compared to the reverse-bias characteristics for VLWIR devices. Issues with passivation were found to be critical.

Cap-layer variations including thermally-evaporated (TE) ZnS, TE CdTe, electron beam evaporated (EBE) CdTe and in-situ CdTe/ZnTe grown by MBE were compared with respect to their effect on As-ion implantation. Channeling effects were observed for thin layers of evaporated CdTe. An optimized thickness of ZnS was found to obtain the deepest As indiffusion after high temperature annealing, and the end-of-range (EOR) depth is linearly proportional to the thickness ratio of a-MCT layer/damage layer.

Inductively-coupled plasma etching of HgCdTe FPAs at cryogenic temperatures—123 K—was described. Fig. 33 shows an example of the etch profile.

A paper was presented on the bulk growth of <111> seeded 75 mm diameter cadmium zinc telluride (CZT) using the traveling heater method (THM) which allows for growth at lower temperatures. The report summarized work on development of epitaxy-ready surface finishing of THM-grown $Cd_{0.96}Zn_{0.04}Te$ substrates. Xray rocking curve values averaged 22 ± 3 arc sec. The crystals were reported to be free of twins and slip and GDMS measurements reported less than 2 ppba of copper impurities.

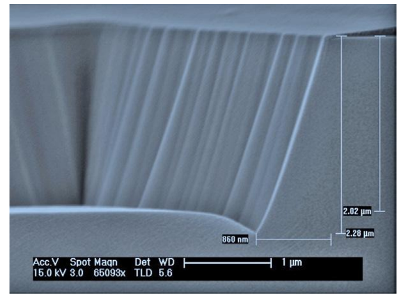

Fig. 33 The profile after an optimized plasma etch.

Uncooled Detectors

Participation in the uncooled session was down this year, largely due to the reluctance of U.S. companies to show their competitive hands, and also due to persistent U.S. government restrictions on release of information to an international audience. Nevertheless, several papers were presented showing advances in absorption, thermal isolation and limitations of pixel size reduction.

Four papers – one from China, two from Japan and one from the U.S. – addressed wavelength-selective absorption using plasmonic structures. One of the Japanese papers was presented in the poster session. These papers showed the dependence of the absorption spectrum and absorption efficiency on the feature sizes of the structures in the absorbing layer. The key advantage of these structures is that different pixels can have different spectral and/or different polarization characteristics within the same array, thus facilitating multi-spectral imaging in a manner akin to color visual sensors and displays. A disadvantage is that the plasmonic structures are generally more massive than the usual semi-transparent thin films used in resonant absorbers, and therefore detectors using them have somewhat longer thermal time constants.

Another poster paper from Japan explored the potential use of graphene as infrared detector. The paper showed that the use of a plasmonic metamaterial absorber could substantially enhance the ordinarily low absorption coefficient of graphene.

A presentation from Germany described a novel nanotube thermal isolation structure. The structures are vertical rather than the usual lateral structures, and they are created by coating the walls of narrow vias between the top of the detector and the substrate. The multilayer coatings within the nanotubes provide both mechanical support and electrical contact, while also providing thermal isolation. This method virtually eliminates the loss of active area usually associated with excellent thermal isolation, but, at first glance, limits available thermal isolation by the fact that the length of the nanotubes is limited by the resonance requirement of the absorber. This apparent limitation, however, is overcome by locating the mirror on a pedestal underneath the pixel instead of its conventional location on the substrate. This allows the nanotubes to be lengthened, limited only by the process for their deposition.

Videos in a U.S. presentation clearly demonstrated the theoretical benefits attainable by continued reduction of pixel size well below the diffractive blur size, even in uncooled detectors. The paper showed that, in the absence of noise considerations and geometrical aberrations, improvement persists until the Nyquist frequency and the diffraction cut-off frequency coincide. Uncooled IR technology innovation continues, and improvements are sure to continue the expansion of the use of microbolometers into applications formerly reserved for cooled FPAs having much higher performance. Multi-spectral FPAs, with the associated loss of performance on a per-pixel basis, will likely drive raw performance improvements of uncooled.

Smart Processing

This session primarily covers advances in detector readout technology such as digital pixels as well as including functionality beyond simple signal/image acquisition in the focal plane circuitry.

An RF network comprised of photoconductive detector elements was described that can locate an area being illuminated. The detector elements, when illuminated connect an upper layer of RF transmission lines to a lower layer of RF transmission lines.

A digital ROIC implementing Time-Delay and Integration (TDI) for 30 µm pixel pitch and 30 mW power consumption previously was reported to be improved

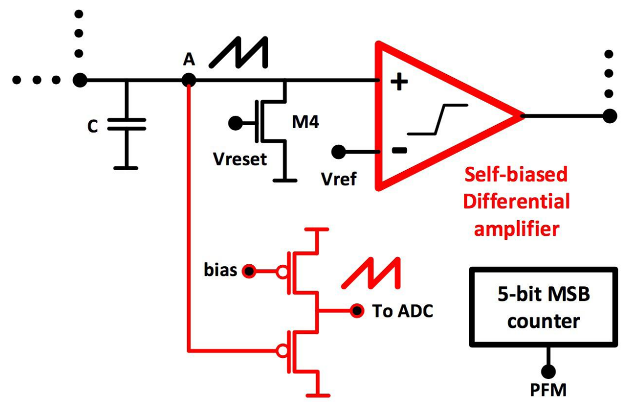

Fig. 34 Schematic including modifications to the PFM pixel include the addition of a source follower and the use of a power efficient self-biased differential amplifier instead of the comparator. The proposed modifications are highlighted in red.

to 15 µm pixel pitch and 20 mW power consumption. Simulation results were carried out for a 90 × 8 format.

A digital pixel using Pulse-Frequency Modulation (PFM) was described that implemented the residue measurement off-pixel using a column ADC in order to employ this technology in smaller pixels. Fig. 34 shows the modified digital pixel schematic. This development is projected to extend this type of ROIC to 15 μm MWIR pixels.

CMOS ROIC design parameter extraction for cryogenic operation was described. The method used is based on the measurement of inversion charges forming the transistor channel and, therefore, is insensitive to low temperature effects related to transport phenomena, like freeze-out effects. Fig. 35 shows the model with extracted parameters compared to NMOS data.

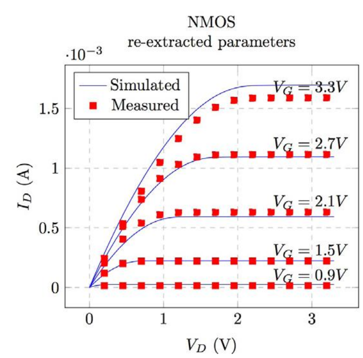

Fig. 35 Measured and simulated $I_D \times V_D$ for NMOS transistors with W = L = 25 µm at 77 K with parameters extracted at 77 K.

Testing of an ASIC that is designed to connect to one or more readout integrated circuits (ROIC) in image sensors based on HgCdTe was reviewed. The ASIC provides all the necessary readout functions to operate an ROIC for a large scale focal plane array, such as: a programmable sequencer, analogue-to-digital converters, power supply regulators, programmable gain amplifiers, programmable bias and reference voltages and monitoring inputs.

1/f Noise Update

It was claimed that the omission of the Navier-Stokes equation from the description of semiconductor carrier transport has hidden the reason for the universal observation of 1/f noise in these materials. The Navier-Stokes equations predict turbulent flow. Turbulent flow has been shown to have a 1/f spectrum for fluctuations in mass transport which may provide a natural explanation for 1/f noise. Fig. 36 shows the spectrum of mass flow fluctuations modeled from a jet impinging upon a reservoir. Fluctuations were evaluated at a distance of 20 jet diameters from where the jet enters the reservoir.

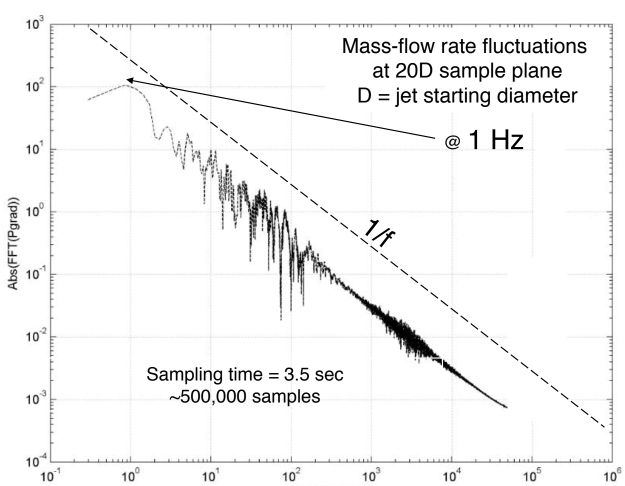

Fig. 36 Spectrum of mass flowrate fluctuations sampled from a turbulent flow.

Applications

Presentations focusing on applications of the various infrared technologies in systems and subsystems were presented in Sessions 2 and 3. As applications are the main drivers for technology R&D, references to system applications can be found throughout the Proceedings.

A national laboratory reviewed three recently developed air- and space-borne sensor systems. One was an airborne hyperspectral emission spectrometer developed to support hyperspectral measurements from a low Earth orbiting satellite. The second system, a multispectral radiometer, is being developed for use on the International Space Station. Its main purpose is to monitor the temperature of Earth vegetation. Fig. 37 shows results from monitoring water stress in the U.S.. The third system will investigate changes in temperature and composition of the Martian atmosphere. The measurements will be made while the sensor system orbits the planet.

A university institute for geophysics and planetology presented a prototype hyperspectral imager based on a Sagnac interferometer spectrometer—see Fig. 38—to be installed on a microsatellite platform. Its low mass and power consumption combined with absence of moving components make it ideal for low-orbit space applications. It operates in the MWIR spectral region and will, in one version, employ an uncooled microbolometer.

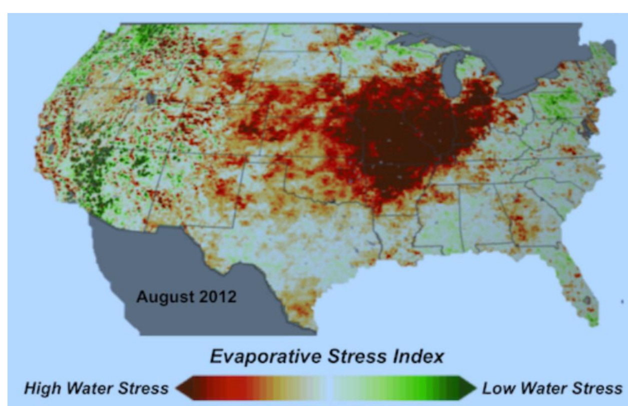

Fig. 37 Map of the 2012 drought in the United States showing differences in water stress. Red areas indicate high water stress (drought conditions) and green areas indication low water stress (non-drought conditions).

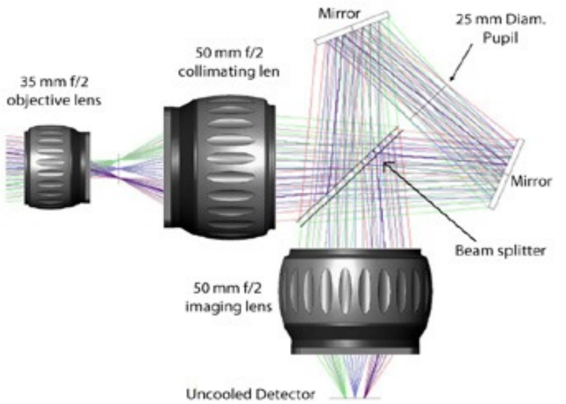

Fig. 38 The Sagnac interferometer with collimating and imaging lenses.

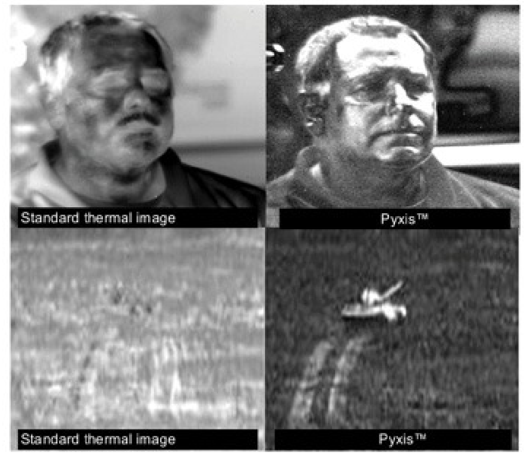

Fig. 40 Examples of polarimetric images (right-hand column).

A European company has developed an airborne IRST system designed to satisfy the demanding requirements of 5th generation fighter aircraft—see Fig. 39. Acquisition of targets at distances compatible with a beyond-visual-range missile launch was facilitated by improved hardware – optics, detector and processor. The most important technological improvement was in the development of processing algorithms which investigate target signatures, including variations in color and brightness, in order to filter out false alarms. Detector non-uniformities were, at times, found to be the limiting factor for detection of distant targets.

One company highlighted challenges faced in development of infrared technologies for missile applications. Attention was focused on very compact Joule-Thomson-cooled detectors.

The second applications session described three surface-based infrared imagers. Each imager benefitting from optimizing its design around a specific technology.

Fig. 39 Embedded version of the IRST during flight trials.

One company presented a handheld or helmet-mounted polarimetric imager for improved detection of man-made targets in clutter and recognition of facial characteristics—see Fig. 40. The microbolometer-based imager uses a polarization microgrid array integrated into the optical system and captures all polarization states simultaneously. Presented data showed immunity to motion artifacts.

The second ground-based application presentation highlighted the processing software of thermal binoculars. The processor provides interfacing with laser rangefinder, digital compass and GPS. The geolocation data received from the "software-defined camera" helps minimize occurrences of friendly fire and civilian casualties. The primary sources of error in geolocation was discussed—see Fig. 41.

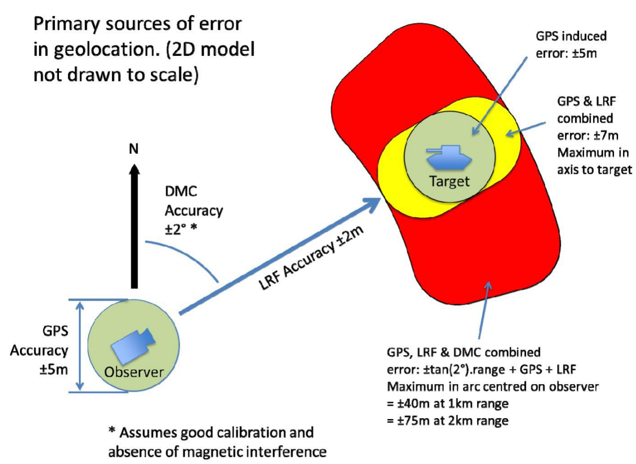

Fig. 41 Primary sources of error in geolocation illustrated in a 2D model.

A Word from the Master

Roger DeWames was the speaker for this session. He reviewed an assortment of IR materials and devices covering the visible to VLWIR spectral region. Topics included InGaAs SWIR characteristics and ways to improve these devices. InSb homojunction devices were covered next, followed by MWIR HDVIP devices. Finally, double-layer MWIR and LWIR were considered and their limitations and potential for improvement were reviewed.

Keynote address

Dr. Karl-Heinz Rippert of the German Defence Agency gave the keynote address on the role of infrared technologies and systems in the German Federal Defense Forces. He reviewed plans to reduce pixel size to 5 μm and increase the FPA format to 2048×1536 while keeping the dewar size fixed. This development is being supported in order to improve the identification of asymmetric threats. Higher operating temperature with reduced power consumption was also featured in the plans. SWIR development for low-light and active detection will be an important part of future technology. Finally, data processing from sensors, international networking, and joint data bases were noted as important components in defense force modernization.

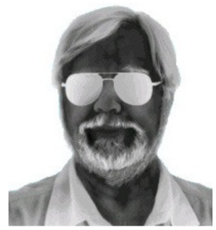

Paul R. Norton

Bjørn F. Andresen

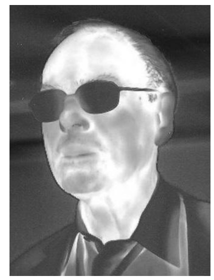

Gabor F. Fulop

Charles M. Hanson

Federal Office of Bundeswehr Equipment, Information Technology and In-Service Support

The Role of Infrared Technologies and Systems in the German Federal Defense Forces

Keynote Presentation: SPIE Infrared Technology and Application XLII

Bundeswehr
Wir. Dienen. Deutschland.

Dr. Karl-Heinz Rippert
Chief
Optics / Optronics Branch

BAAINBw

Bundeswehr
Wir. Dienen. Deutschland.

BAAINBw

Bundeswehr
Wir. Dienen. Deutschland.

BAAINBw

Outline

Bundeswehr
Wir. Dienen. Deutschland.

Optronics

- Main Targets / Research
- Technology Lines, Key Technologies and Trends
  - Semiconductors
  - Sensors and Detectors
  - Processing
  - International Networking with Joint Databases

19 April 2016 UNCLASSIFIED 4

BAAINBw

Main Targets

Bundeswehr
Wir. Dienen. Deutschland.

- ✓ UV to LWIR components for airborne reconnaissance, surveillance and warning systems, air control and surveillance and harbor protection
- ✓ standardised algorithms for target recognition, change detection and geo-referencing in urban terrain
- ✓ tactical network centric fire support
- ✓ training and simulation in networked environments
- ✓ guidance, command & control in joint international operations
- ✓ tactical reconnaissance mangagement and data exchange
- ✓ hardening of sensors and IT systems against threats
- ✓ conjunction with non military research to increase dual use

19 April 2016 UNCLASSIFIED 5

BAAINBw

Research Topics

Bundeswehr
Wir. Dienen. Deutschland.

Technology Lines / Research

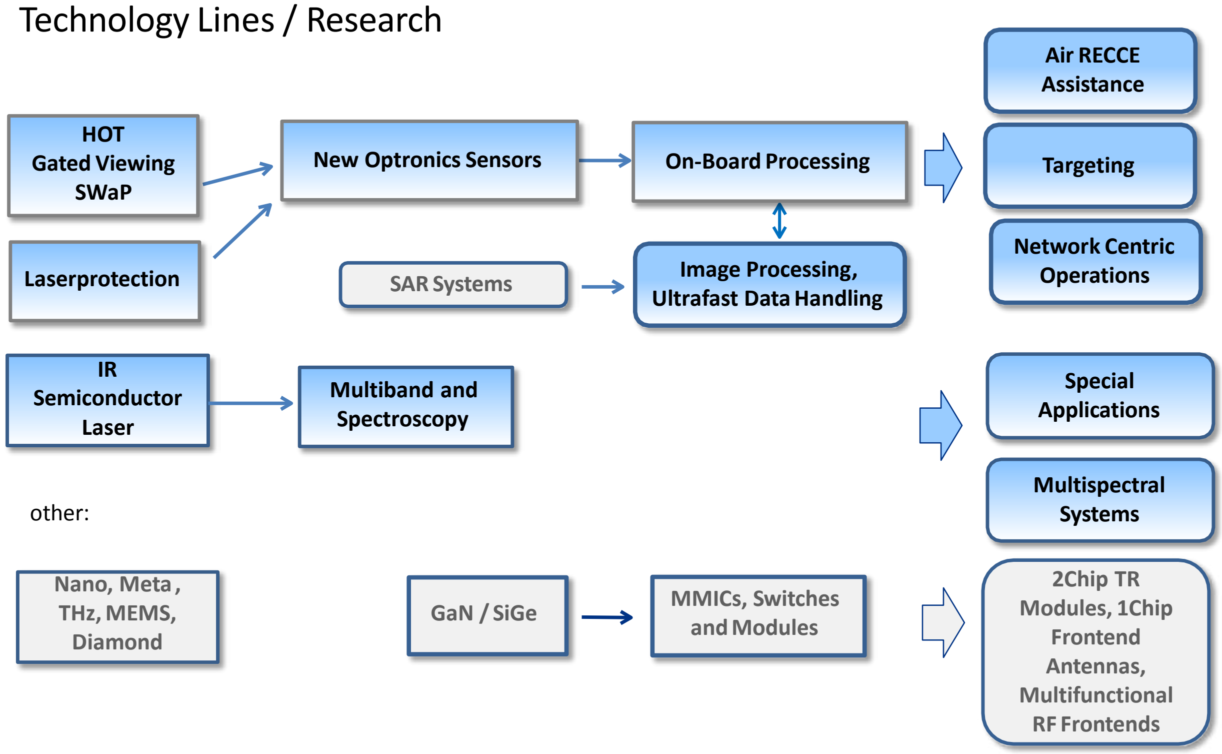

19 April 2016 UNCLASSIFIED 6

BAAINBw

High Definition MCT IR Detectors with Reduced Pixel Size

Bundeswehr
Wir. Dienen. Deutschland.

small pixel, large format
„more pixel on target"

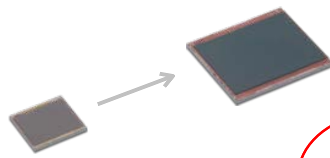

TV/4 ✓
384x288, 24µm
2000

VGA ✓
640x512, 15µm
2010

XGA ⌛
1024x768, 10µm
2015

SXGA ✓
1280x102

HD ⌛
1280x720
12µm

SXGA+
e.g. 1440x1080, 7µm
2020

QXGA
e.g. 2048x1536, 5µm

keep detector area size ~ const.

use of identical dewar, ‚form fit IR-module'

challenges:
- hybridization, In-bump technology
- pixel rate, bandwidth
- power consumption of ROIC
- charge handling capacity
- MTF

advantages on system level:
- increased range performance while keeping outlines
- same range performance with more compactness
- interfaces and functionality similar

19 April 2016 UNCLASSIFIED AIM 7

BAAINBw

High Definition MCT IR Detectors with Reduced Pixel Size

Bundeswehr
Wir. Dienen. Deutschland.

Improved Identification of Threats and Asymetric Scenarios

HD IR-Module 1280x1024,15µm pitch at MWIR und LWIR

Improved CROP
- recognition of threat potentials
- of persons
- situation awareness of larger area at same resolution

Way Ahead of IR-Technology in full HD:
- 1920 x 1080 pixels with10µm pitch
- ROIC technology with large capacitor for high dynamic performance

detail with equivalent resulution of complete image

detail with higher resulution as complete image

19 April 2016 UNCLASSIFIED Fraunhofer IOSB 8

HOT IR - Modules

BAAINBw

Bundeswehr
Wir. Dienen. Deutschland.

Reduction of Size, Weight and Power (SWaP) ⟹ High Operating Temperature MCT MWIR Detectors

	120K	140K	160K	180K	200K

HOT GEN 1

HOT GEN 2

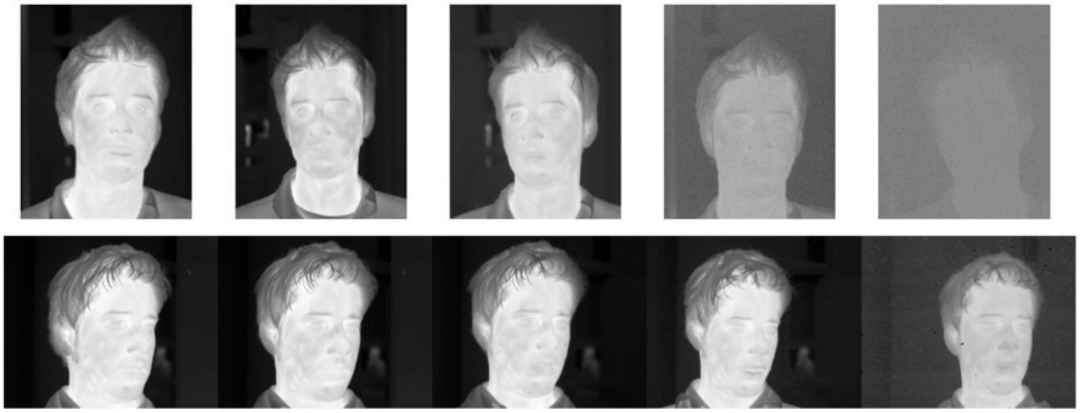

F/3.5, 640x512, 15µm pitch, λ_{CO}= 4.75 µm @ 160K

Standard two point NUC and pixel replacement; histograming mode

- HOT GEN 1 (120K): good image quality up to ~160K
- HOT GEN 2 (140K): good image quality up to ~180K
- challenges:
  - reduce dark current
  - decrease number of defective pixels at elevated temperatures

SWIR Detectors for Low-Light Level Imaging

BAAINBw

Bundeswehr
Wir. Dienen. Deutschland.

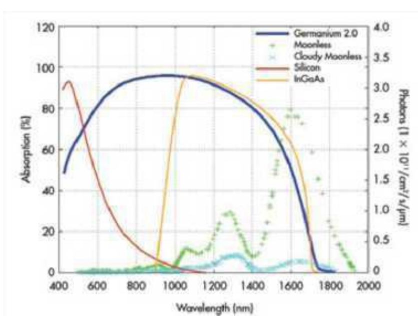

night glow @ night, no moon, no clouds (green)

night glow @Nacht no moon, clouds (zyan)

picture: no moon, no clouds, SWIR 1.8 cooled
reflexion 5%, 20%, 50%, 90%, 95%
distance targets150m, forest 300m

0.9µm – 2.5µm night glow photos compared to thermischen photons. In atmospheric window 2.0µm – 2.5µm thermal radiation is dominating.

With SWIR2.5 imager (cooled) NETD to 150mK at TBB ~ 20°C possible. Real system comes with 1.8µm cutoff warm filter.

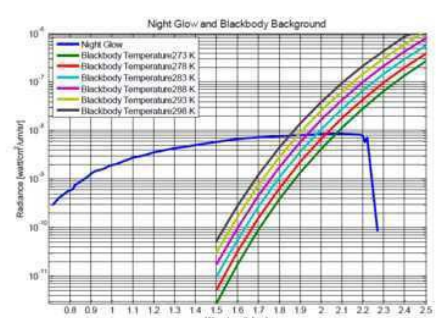

Figure 1 – Night glow radiance (reproduced from [2]) in comparison with blackbody background radiation

XXXV

BAAINBw

SWIR Detectors for Low-Light Level Imaging

Bundeswehr
Wir. Dienen. Deutschland.

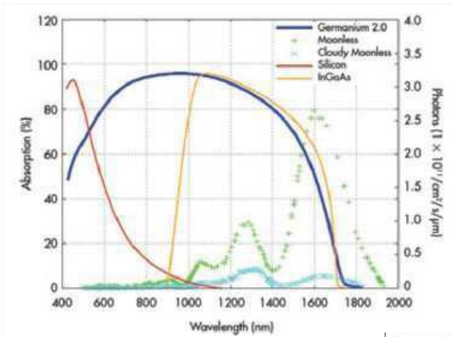

Night Glow at moonless night without clouds (green)

Night Glow at moonless night and clouds (zyan)

Picture : moonless without clouds Night Glow SWIR 1.8 cooled scheme with 5%, 20%, 50%, 90%, 95% Reflexion sceme in 150m, forest in 300m distance

0.9µm – 2.5µm Night Glow photon vs thermal photons. Atmospheric window: 2.0µm – 2.5µm with dominating IR radiation. SWIR2.5 cooled IR image NETD ~150mK at ~ 20°C ambiance temperature.

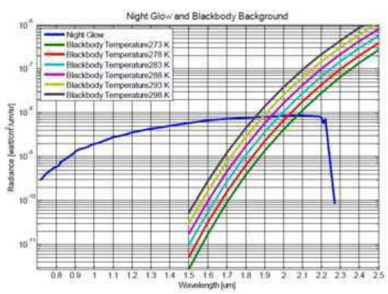

5% 20% 50% 90% 95%
Night Glow, moonless night
CMT 1.8µm

Trend: MESA to SWIR Planar structures

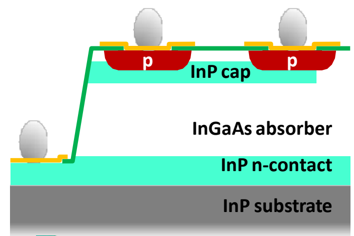

BAAINBw

SWIR Detectors for Low-Light Level Imaging

Bundeswehr
Wir. Dienen. Deutschland.

SWIR Detectors for low-light level imaging

SWIR camera CMT
(0,9µm – 1,8µm)
FoV 6,1° x 4,9°
640 x 512 pixels

SWIR by CMT detector at night, car lights improvement by local contrast enhancement

tower 1500m
Class 1 LRF
1,25 mrad x 0,1 mrad

linear grey values

lokales histogramming for grey values

2D SWIR Detector for active imaging (Laser-Gated-Viewing)

Pros vs passive imaging:

- high identification range to discriminate threat / no threat
- recognise shapes / contoures vs. background
- depression of foreground disturbances (e.g. camouflage nets, smoke, fire)

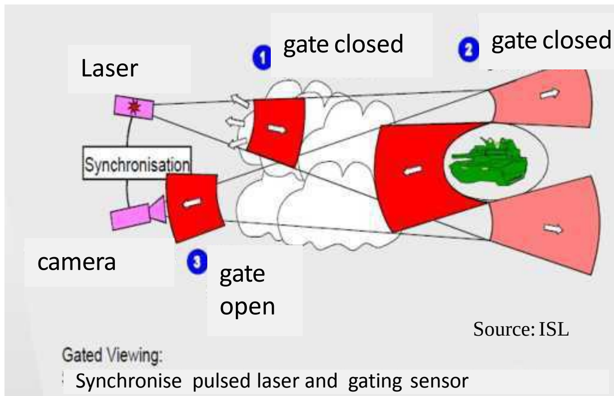

2D SWIR Detector for active imaging (Laser-Gated-Viewing)

Gated Viewing advantage:

- Imaging thorugh smoke without distraction
- Day / night application
- Improved target identication (looking throug class windows)

Further technology R&D:

- High sensitive detectors => APDs at Gain >1
- ROIC with gating capability, and precise time gating (trigger by laser und programmable gate)

VIS Channel SWIR Gated

source: ISL, 1.5µm laser gated viewing, recognition of person through smoke

source: ISL, 1.5µm laser gated viewing, harbour, 1km distance

BAAINBw

Dual-Band MCT IR Modules

Bundeswehr
Wir. Dienen. Deutschland.

<u>Preliminery design</u>:

- detector format: 640x512 pixels
  20 µm pitch
  l_{co} = 3-5µm & 8-10µm
  MBE-MCT on CZT
- pixel-design back-to-back
  ⇒ spatial coincidence
  ⇒ sequential integration

⇒

<u>Final design</u>:

1280x720 pixels
12 µm pitch

- current development
- MBE-MCT on GaAs

IDCA with adaptive cold shield aperture
➢ F/2 for LWIR and F/4 for MWIR

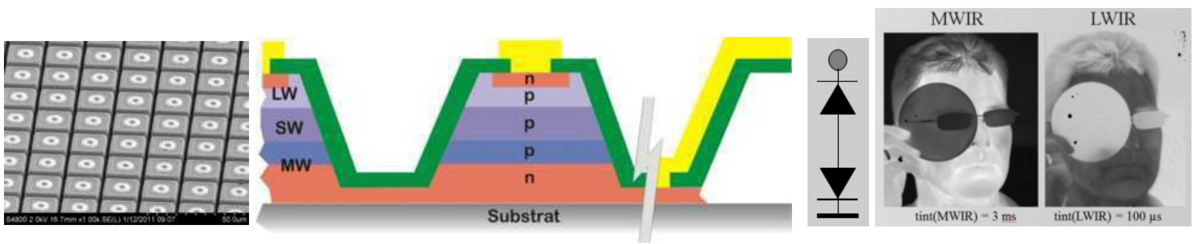

19 April 2016 UNCLASSIFIED Fraunhofer IAF 16

BAAINBw

Dual-Band MCT IR Modules

Bundeswehr
Wir. Dienen. Deutschland.

Enhance Reconnaissance Performance by Dual-Band Detectors

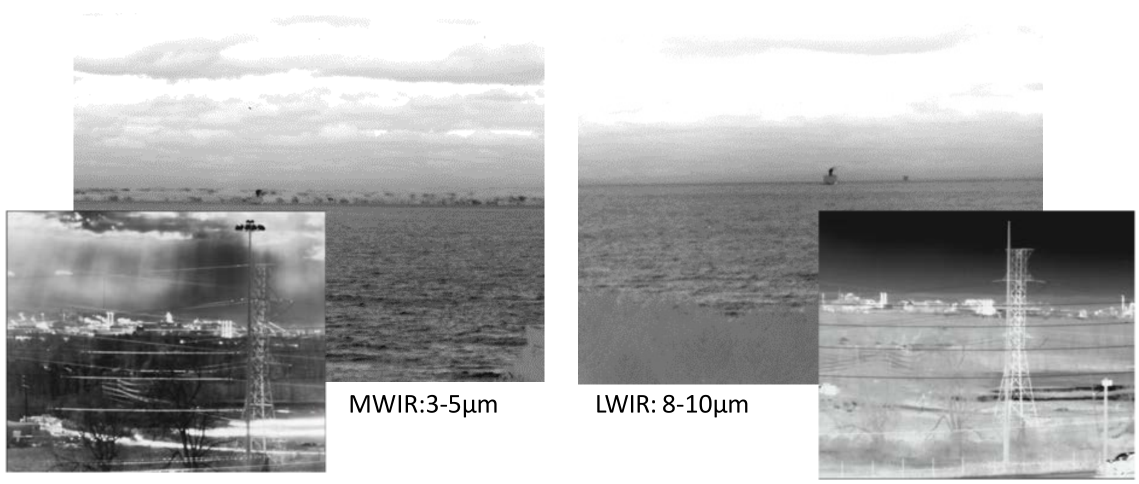

MWIR:3-5µm LWIR: 8-10µm

Advantages of Dual-Band IR Detectors (3–5 µm und 8–10 µm):

⇒ always to choose best band independend from environment conditions
⇒ optimised for operations (detection: LWIR; identification: MWIR)
⇒ enhanced target classification by fusion of different (independend) spectral information
⇒ optimise contrast

 19 April 2016 UNCLASSIFIED Fraunhofer IOSB 17

Processing

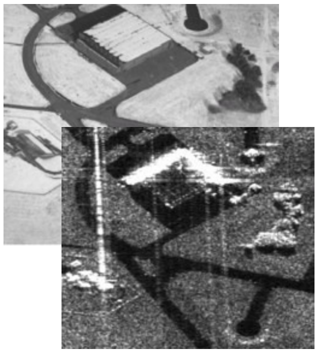

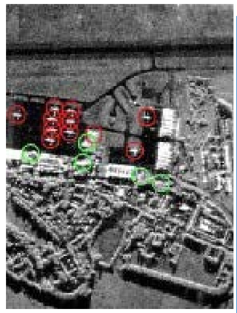

FhG

Aim

- support evaluaters to interprete complexe data from different imaging sources
- improve identification results by combination of methods

Way

- concept to use multisource methods with different levels of automation
- enhance assistance systems
- establish catalog if test signatures
- analyse potential conflicts and learning procedures

Results to achieve

- Interactive assistence system to evaluate optical / IR and SAR images
- Automatic procedures to enhance data for training
- enhanced assistence for sensor management and training

International Networking with Joint Databases

CSD (Coalition Shared Data) Server based on STANAG1 4559
(NSILI-NATO Standard ISR2 Library Interface)

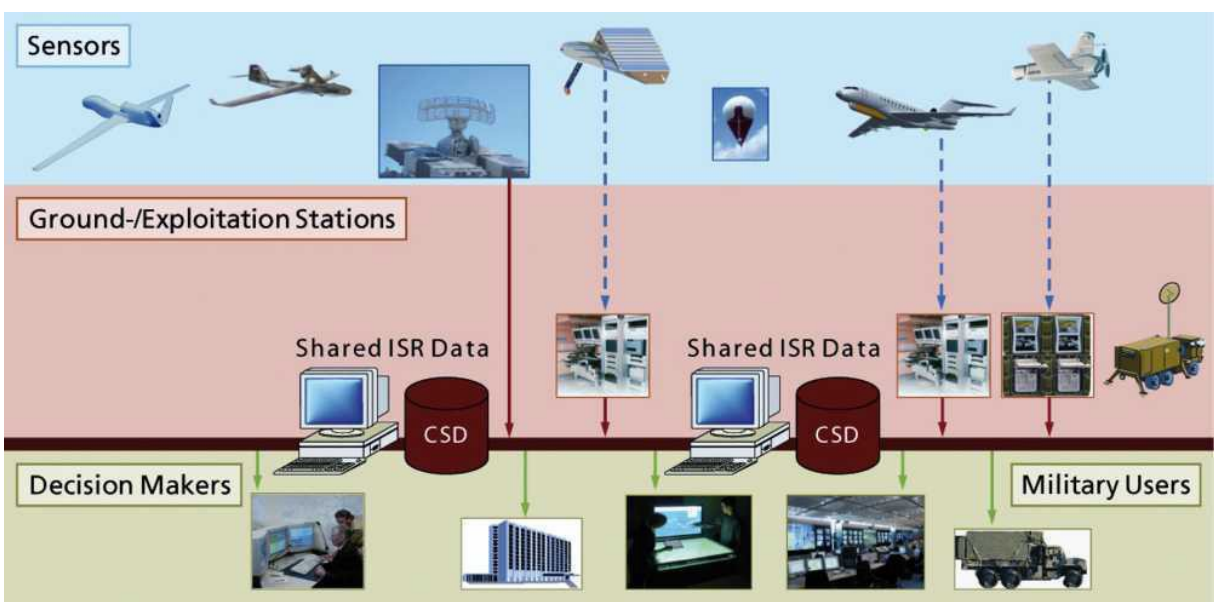

BAAINBw

Bundeswehr
Wir. Dienen. Deutschland.

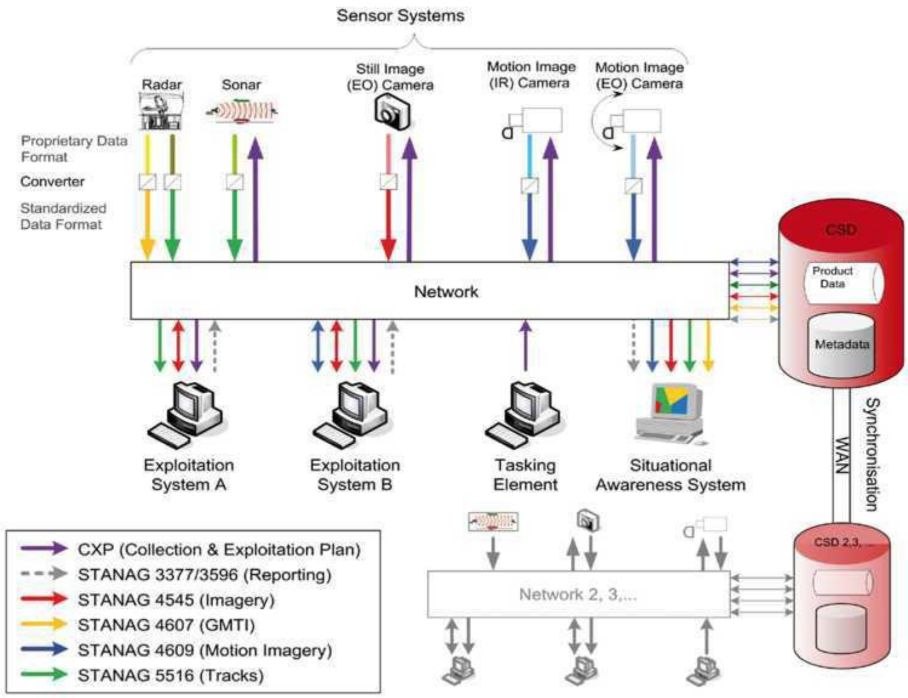

Exploitation of systems store relevant metadata and products in common formats

Interoperable architecture enables data analysis, international coordination and networking

BAAINBw

Bundeswehr
Wir. Dienen. Deutschland.

Thanks AIM Fraunhofer IOSB Fraunhofer IAF ISL

Dr. Karl-Heinz Rippert
Regierungsdirektor
Section Leader

KarlHeinzRippert@bundeswehr.org
phone.: (+49) 261 - 400 - 18370
fax: (+49) 261 - 400 - 18552
mobil: (+49) 151-1955 1506

Federal Office of Bundeswehr Equipment, Information Technology and In-Service Support
Optics / Optronics for Ground Systems, Infanterist der Zukunft IdZ

BAAINBwU5.5@Bundeswehr.org
Ferdinand-Sauerbruch-Strasse 1
D-56057 Koblenz
Internet: www. baainbw.de